Medical University "Prof. Dr. Paraskev Stoyanov"

Faculty of Medicine

Department of Imaging, Interventional Radiology and Radiotherapy

Innovative breast phantoms for studying image quality in modern mammographic techniques

Yanka Ivanova Baneva

THESIS SUMMARY

Research supervisors:

1. **Prof. Boyan Dobrev Balev, DM**
2. **Assoc. Prof. Kristina Stanimirova Bliznakova, PhD**

Varna, 2022

INTRODUCTION

Incidence of breast cancer

Breast cancer is the most common worldwide cause of death in women – 460 000 deaths per year (Edited by Georgi Dimitrov, Ivan Gavrilov, Teofil Sedloev, 2014). The risk of breast cancer is more significant in women with a family history of the disease, women who have already developed breast cancer, women with a denser breast structure, women with early menstruation or those with late menopause. The risk of developing breast cancer also increases with age.

Breast composition

Higher breast density is associated with an up to 6-fold increased risk of breast cancer compared to women with lower breast density (Saftlas et al., 1991; J. H. Chen et al., 2011). Diagnosing dense breasts during mammography is difficult, with 20 – 30% of cancer cases not showing up on mammograms (Cheung et al., 2014).

Types of mammary gland tumours

Breast cancer is generally divided into non-invasive – when the tumour cells have not yet managed to move into the tissue around them, and invasive – when the cells have already moved into the surrounding tissue. The first type includes ductal carcinoma in situ and lobular carcinoma in situ. If ductal carcinoma in situ is not treated, it can develop into invasive ductal carcinoma, which occurs in 70% of breast cancers. The detection of lobular carcinoma in situ is an alerting sign that the patient may develop breast cancer in the future, but this is rare. The other type of invasive breast cancer is lobular carcinoma. It occurs in about 10% of breast cancers (Kerry McGinn, 2007). The possibility of several cancer foci characterises it, and this type of breast cancer is considered to have a better prognosis for survival.

Calcification and benign or malignant pathologies attract attention when reading a mammogram. Pathologies with absorption properties close to those of glandular tissue are groups of cells with an abnormal structure called asymmetry in a single projection. Their shape can be round (a), oval (b), or irregular (c) (Figure 1.1). These pathologies are found anywhere in the breast, and their size is 1 – 4 cm.

a b c

Figure 1.1. Shape of benign and malignant pathologies: a) round shape, b) oval shape, c) irregular shape

Pathologies' margins – lesion borders, are 5 main types (Figure 1.2): a) circumscribed, b) obscured, c) microlobulated, d) indistinct, and e) spiculated. If the margins are well-defined, this is a benign finding.

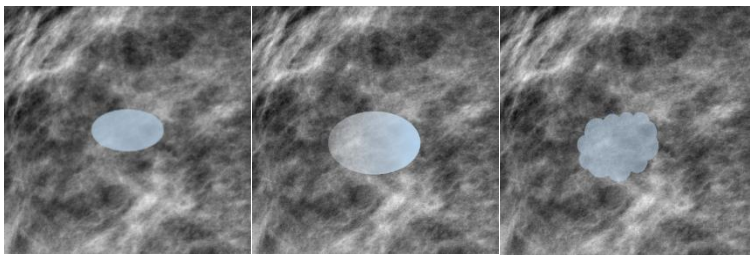

a b c

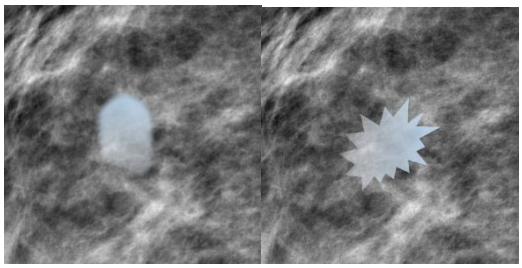

d e

Figure 1.2. Lesion margins: a) circumscribed; b) obscured; c) microlobulated; d) indistinct, e) spiculated.

When the margin is hidden by superimposed fibroglandular tissue, ultrasound is recommended to be used to define the margin better. When the margin is indistinct or microlobulated, the finding is suspicious, while a spiculated margin with radiating lines from the mass is a highly suspicious finding on mammogram reading. The expected attenuation of X-ray radiation of an equal fibroglandular tissue volume is called density (Figure 1.3). High density is associated with malignancy.

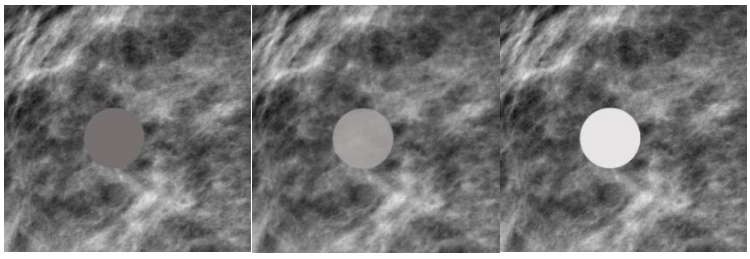

a b c

Figure 1.3. Density of the lesion when the x-ray beam passes through the tissue: a) low density, b) equal density, c) high density

Calcifications are small accumulations of minerals in cells resulting from a benign or malignant process, with sizes from 0.1 mm to 1 cm. They are of particular interest in breast cancer research. Their characteristics are presented in Table 1.1 (Smithuis, 2013).

Table 1.1 Characteristics of calcifications

Locations	Explanations
Location	Might be found: • in or around the milk duct; • • in the lobules; • • in blood vessels; • • in the skin; • in the interlobular connective or fatty tissue; • • in pathologies.
Size	• 2 mm or more; • • smaller than 1 mm.
Morphology	The shape and margins are like those in pathologies.

According to the American College of Radiology (ACR), skin, vascular, coarse, large rod-like, round or punctate (< 1mm), rim, dystrophic, milk of calcium and suture calcifications are most likely to be benign. With suspicious morphology are:

• the amorphous, coarse heterogeneous calcifications with irregular, conspicuous calcifications, measuring between 0.5 mm and 1 mm, tending to coalesce;

• calcifications, with diverse shapes, without linear branching forms, usually < 0.5 mm;

• linear irregular calcifications that may be discontinuous and sometimes branching, usually < 0.5 mm.

None of the parameters is used alone to determine the type of the finding – benign or malignant, rather the correlation between them. Round, oval, or individual lesions with sharper, well-defined margins, measuring less than 1.5 cm, containing almost entirely adipose tissue, are most likely benign.

Malignant lesions have high density, spiculated margins, and illegible, irregular, or fuzzy contours. Benign calcifications are usually scattered and have a uniform shape and density. Macro-calcifications are usually large and round and almost always benign. Malignant calcifications are usually irregular in shape, size and distribution. They are usually smaller than the benign ones and are of particular clinical significance when found in clusters of five or more per square centimetres (Sickles, 1986). Calcifications that are not found in glandular tissue are usually benign.

Breast carcinoma is staged according to the 7th revision of the TNM classification of the American Joint Committee on Cancer (AJCC) and the Union for International Cancer Control (UICC) since 2010.

Physical examination and imaging tests of the breast are the minimum tests required to determine the T, N, M categories (NATIONAL GUIDELINES for Breast Cancer Management, 2013).

Types of breast cancer examinations

An essential prerequisite for successful breast cancer treatment is the early diagnosis (Kozhuharov, 2007). The breast's X-ray picture depends on the tumour's morphological type, histological structure, tumour size and the state of the mammary gland (Bozhkov, Toma, Dobreva, 1982). Because of this, examination devices should have high sensitivity so that the resulting image can provide the necessary and correct information about the condition of the patient's mammary gland.

Mammography is used mainly for screening and diagnosis. The screening program aims to examine patients without symptoms or suspicions of breast cancer, with the idea of an early diagnosis of tumour formations. Diagnostic mammography examines patients with family history or suspicions of breast cancer.

Ultrasound

Up to the age of 40, breast cancer examination is recommended to be conducted by ultrasound. In this case, the differences in the amplitude and intensity of ultrasound when passing through media of different densities are used. The intensity distribution of the reflected pulses from the ultrasound in the plane realises the echographic image.

Magnetic Resonance Imaging

In cases suspicious of breast cancer after mammography, to stage it or determine its spread in the breast, to follow the outcome during treatment, magnetic resonance imaging (Figure 1.4) can also be used (Singh et al., 2008).

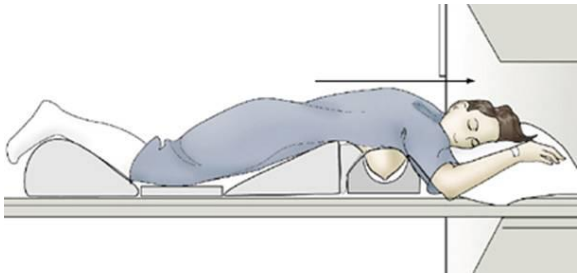

Figure 1.4. MRI

Copyright http://weill.cornell.edu/mri/MRI/Chest/breast_mass_mri.htm

PET/CT

Positron emission computed tomography (PET/CT) is used when disease recurrence is suspected or metastases in the patient's body are suspected (Figure 1.5) (Singh et al., 2008).

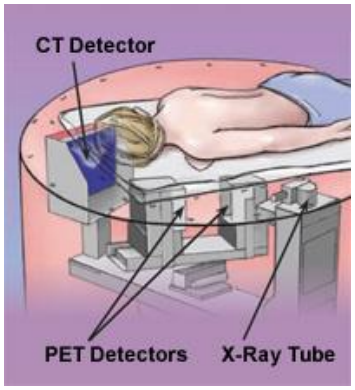

Figure 1.5. PET /CT

Copyright:https://www.ucdmc.ucdavis.edu/synthesis/issues/fall_2008/features/4.html

Mammography

Mammography is the most widely used screening method for breast cancer. In conventional mammography, the mammary gland is examined with the help of X-ray radiation, and the breast is pressed between a plastic plate and an X-ray cassette containing X-ray film or a digital detector (Figure 1.6). Two projections are most commonly used: mediolateral and craniocaudal. Two projections examination reduces the possibility of a non-readable image due to artefacts (Sickles, 1998). In digital mammography, the image obtained through X-rays is converted into an electrical signal through a solid electronic sensor. The resulting image can be viewed directly on a screen and printed on a particular film, similar to conventional mammography.

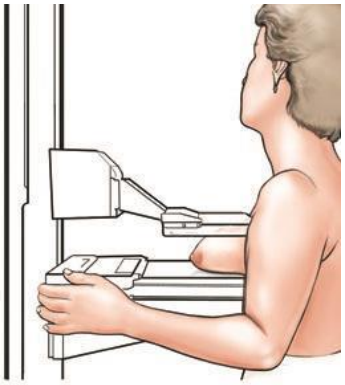

Figure 1.6. Mammogram examination

Copyright: https://my.clevelandclinic.org/health/diagnostics/4751-what-if-they-think-they-see-something-on-my-mammogram

Three-dimensional mammography

Tomosynthesis creates a 3D image of the breast obtained in the mediolateral and craniocaudal planes. In contrast, the breast is compressed as in a conventional mammogram (Figure 1.7), and the source of ionising radiation is rotated around it at a certain angle, usually in the range of 15º – 60º; between 10 and 25 low-dose breast images are taken. The resulting images are reconstructed to avoid tissue overlapping in the image, which happens in conventional mammography (P. Coop, C. Cowling, no date) (Cockmartin et al., 2015).

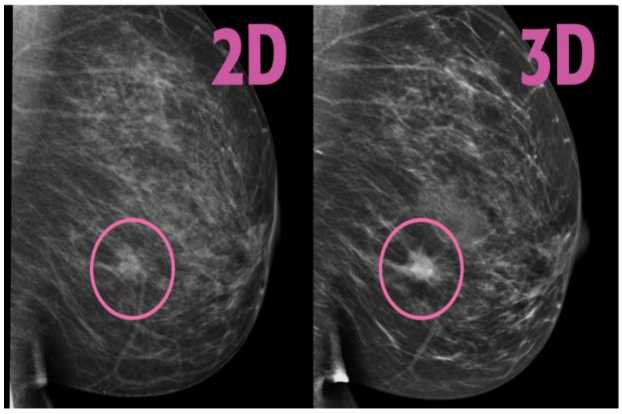

Figure 1.7. Comparison between conventional mammography and tomosynthesis

Copyright: https://www.rmipc.net/tomosynthesis/

Computed Mammography CT

In the CT scan shown in Figure 1.8, the patient lies prone on a bed with a specially made opening in the middle for the breast to be examined. In this way, the source of ionising radiation irradiates only the examined breast without irradiating other parts of the body.

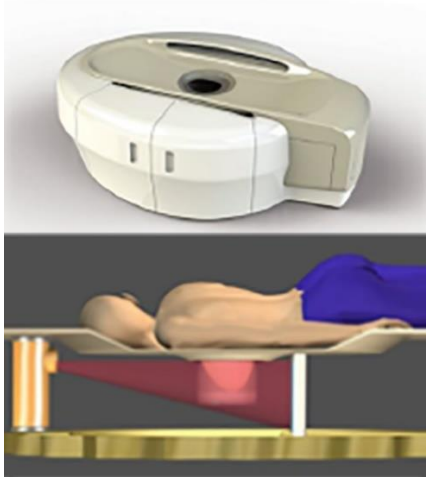

Figure 1.8. Computed tomography of the breast
Copyright: https://scanmed.com.sg/breast-ct-0/

This method can offer very good differentiations between soft tissues and dynamic contrast studies of the breast, but with insufficient spatial resolution and a higher radiation dose. (Schulz-Wendtland, 2013)

Contrast-Enhanced Spectral Mammography

Angiogenesis accompanies tumour growth or metastasis (Carton et al., 2008). By introducing a contrast agent into the patient's body, the better absorptive capacity of the tumour cells will be depicted much more clearly as a result of angiogenesis. Contrast-enhanced spectral mammography (CESM) is as accurate as MRI and more accurate than DM in detecting cancer (Francescone et al., 2014). CESM can be applied to almost all patients requiring the test. It is carried out as follows (Figure 1.9): about 3 ml/s of iodine-based contrast agent is injected into the patient's antecubital vein, an approximate dose of 1.5 ml/kg body weight. Not earlier than 90 s after the end of the injection, a bilateral projection is made with low-energy (26-32 kVp) and high-energy (45-49 kVp) x-ray, selected to be larger than the absorption K-edge of iodine (33.2 keV). The procedure usually takes 7 – 10 min, as long as the examination during DM. Patients must hold their breath during the examination to avoid motion artefacts (Cheung *et al.*, 2014; Luczyńska *et al.*, 2014; ElSaid *et al.*, 2015). Images are obtained by the weighted logarithmic subtraction method: $\ln(C_1)$ – $R\ln(C_2)$, where

C_1 and C_2 are the pixel values at two energies and R is the weighting factor (Philip Palin-Dendy, 2011).

Low-energy images during CESM are obtained using molybdenum and rhodium for targets and filters of these materials, with the voltage ranging from 26 kVp to 31 kVp, below the absorption K-edge of iodine, which reduces the possibility of a photo-effect (Francescone et al., 2014). The obtained image gives maximum contrast of the soft tissues

A Mo target with a copper-layer filter at 45 to 49 kVp was used to obtain the high-energy image. Exposure to Mo or Rh was selected depending on the breast thickness. This technical design ensures that the x-ray spectrum is below and above the K-edge of iodine (33.2 keV) for a successful CESM. Acquisition of low- and high-energy images resulted in the generation of a subtracted image that indicated the presence of iodine uptake in the lesions (Lobbes et al., 2013; Cheung et al., 2014)

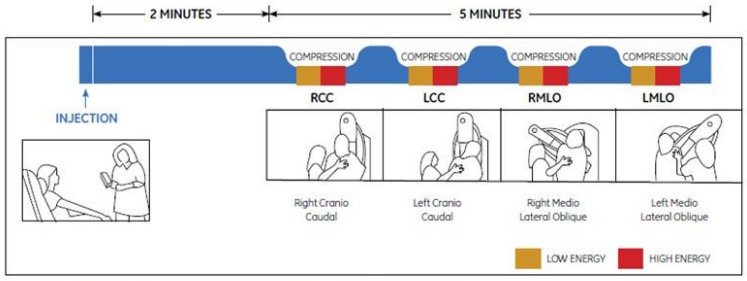

Figure 1. Typical CESM imaging procedure for a bilateral examination with two views per breast.

Figure 1.9. CESM procedure
Copyright:http://www3.gehealthcare.in/en/products/categories/mammography/contrast-enhanced-spectral-mammography

The difference between DM and CESM is the introduction of contrast material in CESM. The patient's position and the value of low-energy radiation in CESM are the same in both procedures (Francescone et al., 2014).

GE CESM is based on a caesium-iodide-based flat panel detector, the image size is 24 cm by 31 cm, and the matrix has dimensions of 2394 x 3062 pixels, with a pixel size of 100 µm. The anode is made of rhodium, with a molybdenum and rhodium filter with a voltage of 26kVp -32kVp for low-energy radiation. High-energy images are taken at 45kVp – 49kVp with a rhodium filter and another copper filter to achieve a spectrum larger than the absorption K-edge of iodine to increase visibility even at lower concentration of iodine.

After the introduction an iodine-contrast substance and the end of the examination, the patient is supervised for about 30 minutes for an allergic reaction. The compression of each breast lasts no more than 15 seconds. After injecting the contrast material, the procedure takes not more than 4 minutes,

which, together with the time for injecting the contrast material, subsequent waiting and the examination itself, is not more than 10 minutes. The received dose varies from 0.7 up to 3.6 mGy, depending on the thickness of the breast (30 – 80 mm) and the breast anatomy (0 –100% glandular tissue). In table 1.2, a comparison between GE CESM and DM is shown.

Table 1.2. Comparison between GE CESM and DM

	Number of patients	Number of detected lesions	Infiltrated lesions	Non-infiltrated lesions	Benign findings
Mammography	150	157	92	12	53
Contrast-enhanced spectral mammography	128	149	101	13	35

CESM detected 16 lesions that were not detected by DM, 10 of which were malignant, and 9 of which were infiltrating cancer. CESM missed 24 lesions compared to conventional mammography, all of which were benign. In this case, CESM is the better method to detect breast cancer, with 20% false-positive and 0% false-negative results compared to 29% false-positive and 6% false-negative results of mammography (Elzbieta Luczynska et al., 2014). One of the critical parameters determining the quality of the image with CESM is the quality of the x-rays and the performance of the energy subtraction method. The quality of the x-rays determines the signal obtained from the iodinated contrast agent and the signal-to-noise ratio (SNR), (Mia, 2012). This necessitates increased quality control over the equipment to ensure image precision.

Advantages and Disadvantages of Breast Examination Methods

An ultrasound scan is helpful in examining the lymph nodes, especially those that can be palpated but do not appear on a mammogram. We may easily distinguish a cyst (filled with fluid) from a solid mass—a benign fibroadenoma or breast cancer, with US. A breast biopsy can also be performed under ultrasound. Ultrasound is affordable, painless, and dose-free for the patient.

The results presented in Table 1.3 show that ultrasound examination of the breast gives sometimes better results than mammography examination. These results depend on the age of the patients – a greater benefit of the ultrasound examination is in women up to 25 years of age and those with denser glandular tissue, which is why ultrasound of the breast is not recommended to be used without another type of examination for breast cancer (Madjar, 2010).

Table 1.3. Differentiation of the types of finding with ultrasound and mammography

	Number of patients	Malignant findings	Differentiation of ypes of findings during ltrasound examination ı %	Differentiation of types of findings during mammography examination in %
Stavros et al. 1995	750	125	98.4	76.8
Moss et al. 1999	559	256	88.9	78.9
Rahbar et al. 1999	161	38	95.0	89.0
Zonderland et al. 1999	4 728	338	91.0	83.0
Berg et al. 2004	258	177	83.0	67.8

MRI is more sensitive than mammography for detecting multiple malignant lesions (Sardanelli et al., 2004). It is used to clarify the diagnosis when a finding has already been found. However, it is less common as a procedure to detect breast cancer due to the high cost of the examination, its duration – sometimes the procedure takes about an hour, during which time the patient must not move, and so far, insufficiently convincing data on the advantage of this method over mammography.

The main issue with PET/CT examination is the low detection rate of small carcinomas (with a diameter of less than 2 mm) or non-invasive types of breast cancer, the relatively low metabolic activity of some types of tumours to the contrast agent used, as well as the low resolution of the method (Yang, Cho and Moon, 2007; Jodłowska et al., 2016).

DM is limited in reading the images obtained, especially in denser breasts, where the surrounding fibroglandular tissue sometimes reduces the visibility of the lesions (Cheung et al., 2014). In other cases, normal tissue may look 'suspicious' on a mammogram, leading to an unnecessary second

examination of the patient. Digital mammography provides better results in detecting breast cancer in perimenopausal women with denser breasts and in women younger than 50 years (He et al., 2015).

Image Acquisition in Conventional Mammography

Different breast structures have minor x-ray absorption differences that can be increased by reducing the anode voltage of the X-ray tube. However, due to the absorption of the rays by the walls of the tube, reducing the anode voltage will not produce an image. Despite the improvements in mammography devices, their accuracy is no greater than 90%, falling to 56% for dense breasts (Cheung et al., 2014). Due to the similarity of the images, breast cancer is often confused with a benign tumour or cyst, and in the case of mastopathy, it can even be missed.

Radiological Description of Breast Findings in Mammography

Despite the advantages of mammographic screening and the anatomical accessibility of the mammary glands, many cases of breast cancer are diagnosed at a later stage in the development of the disease. In the advanced carcinoma process, a complex diagnostic problem remains accurate staging and subsequent adequate assessment of therapeutic options in each specific case (Edited by Georgi Dimitrov, Ivan Gavrilov, Teofil Sedloev, 2014). The detection of breast carcinoma is based on 4 factors derived from the mammogram:

- The specific morphological structure of the tumour;
- The presence of microcalcifications;
- Differences from the normal tissue structure;
- Asymmetry between the corresponding structures of the left and right breast (Jacob Beutel, Harold L. Kundel, 2000).

The main components of the breast are fibroglandular tissue and adipose tissue. Adipose tissue has a lower X-ray penetration coefficient, which is why this tissue appears darker on a mammogram. Lighter areas on the mammogram correspond to fibroglandular tissue (Jacob Beutel, Harold L. Kundel, 2000). A paper published in 1976 revealed the correlation between breast density and the possibility of developing breast cancer, but this relationship has not yet been fully understood. Density indicates the distribution of epithelial and stromal tissues to adipose tissue in the breast. Cancer cells begin developing in epithelial cells, which is why denser breasts are associated with a greater likelihood of breast cancer (McCormack, 2006) (Boyd et al., 2010).

For better depiction of the milk ducts on the mammogram, it is necessary to use a contrast agent since they are surrounded by connective tissue. The main channels are imaged to a limited extent to the

region just below the areola, with the area further imaged as a dense, fan-shaped structure. Vascular structures appear smooth and wavy (Sickles, 1986).

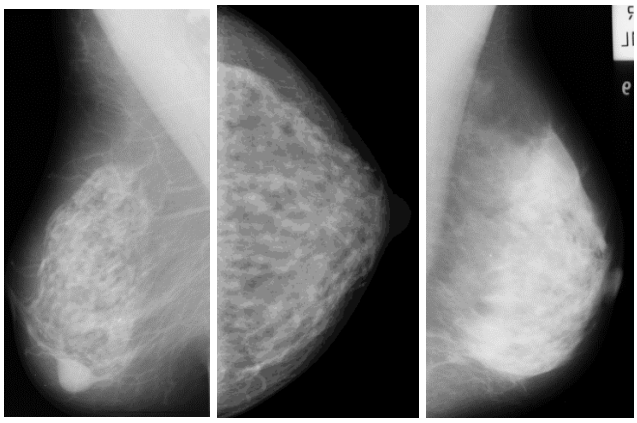

a b c

Figure 1.10. Mammographic images of different breast types: (a – b) moderately dense, (c) dense (Paredes, 1989)

Figure 1.10 shows the fatty tissue depicted as a dark area on a mammogram due to its "transparency" to X-rays, while fibroglandular and connective tissues are depicted with different contrast-bright areas due to the greater absorption of X-rays. The skin attenuates X-ray radiation significantly but is still imaged on the X-ray image due to its small thickness. Cooper's ligaments are depicted as thin curved lines of low intensity. All other anatomical structures are depicted in a shade of white, and benign and malignant tumours appear as bright areas. Calcifications are seen as small, relatively brighter patches than the surrounding tissue (Paredes, 1989).

Radiological Description of Breast Findings in Contrast-Enhanced Spectral Mammography

Digital mammography has much better image quality, contrast resolution, and dynamic range than the conventional method, yet the sensitivity is the same as analogue mammography (Elzbieta Luczynska et al., 2014). Since 2000, using DM in combination with a contrast agent for better carcinoma imaging has been researched, resulting in contrast-enhanced spectral mammography using the energy subtraction method.

Dose Loading

Initial results from a CESM examination show that the dose received by the patient varies from 0.7 mGy to 3.6 mGy, depending on the thickness and density of the breast. This is 1.2 times more than the dose received in conventional mammography. The mean glandular dose (MGD) of low-energy radiation is the same as that of conventional mammography, while the MGD of high-energy radiation is 20% of standard mammography (Dromain et al., 2012). In another study among 118 patients, the

MGD was 1.89 mGy with CESM, and 1.78 mGy with DM, with only a 6.2% increase in MGD. CESM gave the same sensitivity but a better result for the tumour size from DM, which means that DM can be avoided when CESM is scheduled. This will reduce the dose by up to 61%, especially for patients with dense breasts (Fallenberg et al., 2014). Table 1.11 shows values of MGD in 391 images obtained with CESM at a mean breast thickness of 56 mm, and 360 images obtained with DM at a mean breast thickness of 57 mm. The results show that when only low-energy radiation is applied, MGD is almost as in DM (Badr et al., 2014).

Table 1.11. Mean glandular dose in images obtained with CESM and conventional mammography

CESM	Mean glandular dose, mGy	Standard deviation
Image obtained after high-energy radiation in contrast-enhanced spectral mammography	0.65	0.24 – 0.83 (0.23)
Image obtained after low-energy radiation in contrast-enhanced spectral mammography	2.00	0.84 – 3,74 (0.58)
Conventional mammography	1.72	0.74 – 7.82 (0.96)

Contrast-enhanced spectral mammography has proven its efficiency in detecting histologically verified breast cancer cases. Therefore, some authors suggest that low-energy radiation in CESM should be used instead of standard mammography to reduce the dose load for the patient – in case of suspicion after standard mammography, contrast-enhanced spectral mammography is also performed (Francescone et al., 2014).

Sensitivity and Precision

In a study of 52 women between 25 to 74 years of age, 47 of them with invasive ductal carcinoma, 3 with infiltrating lobular carcinoma, one with only ductal carcinoma in situ, and one with ductal carcinoma in situ with stromal invasion, DM detected 42 of all cases, and CESM and MRI – 50 of 52 cases. The size of the lesions, from 4 mm to 67 mm, was detected larger in one of the patients by 1 cm, in the other – by 1.7 cm with CESM, compared to the pathological size, while with MRI, the size of the lesions was detected accurately. MRI appears to be the better method for detecting the location of cancerous growths. In 16 patients with multifocal cancer foci, MRI detected 15 of them to 9 with

CESM. The advantage of CESM over MRI is that within 10 minutes after injection of the contrast agent, the 'enhancement' of the problem area is still visible, whereas, with MRI, this effect subsides very quickly. It is considered that the above is due to the difference in the molecular structure of the substances used in the two techniques (Jochelson et al., 2013).

In 2003, a study of 26 patients tested with CESM was published. The results showed that this method gave 92% sensitivity and 83% precision in detecting cancer formations (Daniaux et al., 2015). In 2011, a study of 120 women showed 92% sensitivity and 56% precision of the same method (Dromain et al., 2011). Results published in 2014 among 89 women showed 92.7% sensitivity and 67.9% precision when tested with CESM (Cheung et al., 2014). Another 2015 –2016 study of 34 women with DM and CESM showed that the sensitivity of CESM was almost 94% to 69% for DM, and the specificity was 91% to 70% in favour of CESM (Saraya, Adel and Mahmoud, 2017).

Some authors have suggested that CESM can be used as a "problem-solving" technique, especially for questionable mammographic or ultrasound results, but due to the slightly higher dose received by the patients, it is not recommended for screening. The side effects when using the iodine-contrast substance are not to be neglected (Daniaux et al., 2015). Its introduction can lead to contrast-induced nephropathy (CIN). According to the Contrast Media Safety Committee (CMSC) of the European Society of Urogenital Radiology (ESUR), a severe "adverse reaction" from a contrast agent occurs within 1 hour of the injection of the agent.

In a study of 325 patients – with a mean age of 62.4 years, the difference between the measured diameter of the tumour finding with CESM and the diameter obtained by histopathological examination was 0.03 mm, while this difference using MRI was 2.12 mm. This means that CESM can be used to determine the exact size of lesions when the hospital does not have an MRI, when the patient does not want to have an MRI examination – for example, in cases of claustrophobia, when the patient has metal implants (Mia, 2012; Lobbes et al., 2015).

The accuracy of breast cancer diagnosis depends primarily on its detection. Improving the examination imaging may improve the early detection of breast cancer. To optimise breast imaging, we should: detect and characterise microcalcification patterns and their morphology, visualise breast parenchyma and slight changes from normal appearance, detect soft tissue masses and determine their size, type and how far they have penetrated the surrounding tissues. The structure of the mammary gland is different depending on age and genetics. The requirements for optimisation are: high spatial resolution, high contrast, and low noise.

AIM

This doctoral thesis aims to create, validate, and use innovative computational phantoms to study the image quality of modern mammographic techniques, such as tomosynthesis and contrast-enhanced mammography, which have the potential to be used for early screening and diagnosis of breast tumours. To achieve this goal, the following specific tasks have been set:

(a) literature review of computational and physical breast models for X-ray 2D, 3D mammography and CESM;

(b) creating computational breast models using specific software tools for X-ray mammography;

(c) creating computational breast models using specific software tools for contrast-enhanced spectral mammography;

(d) validation of computational breast models created as a result of objectives (b) and (c) using specific software tools for X-ray and contrast-enhanced spectral mammography;

(e) use of validated computational models for X-ray tomosynthesis studies;

(f) use of validated computational models for contrast-enhanced spectral mammography studies of the breast.

BREAST MODELS FOR X-RAY IMAGING RESEARCH

Introduction

Computer-generated and physical models, called phantoms, are essential to any medical-related research. They can be used to prove or disprove any statement, thesis, or assumption. The phantom must recreate the studied object as accurately as possible. One particular part is the anthropomorphic phantoms. By definition, anthropomorphic phantoms are physical or virtual objects composed of tissue-equivalent materials that are intended to provide a realistic and accurate representation of the anatomy and properties of tissues, organs, the whole body for use in real and virtual scientific or clinical research, and everyday tasks (Bliznakova, 2018). Realistic and accurate representation means to mimic the external shape and/or internal structures of the modelled human tissue and organs. The properties depend on the properties of the tissue substitutes used in the particular diagnostic application. In X-ray imaging, a tissue surrogate is any material of a certain thickness simulating X-ray attenuation and scattering of human anatomy.

Physical Models

The breast models used to calibrate mammography units are standard – rectangle shapes with a size of 150 mm x 100 mm or 100 mm radius if the shape is of a semi-cylinder while the thickness is the same for both phantoms – 45 mm. The material used is PMMA – to mimic as close as possible the structure of the breast, and different objects are inserted in the phantom to measure the parameters responsible for the image quality (Perry et al., 2007).

Dual-energy contrast-enhanced mammography improves the visibility of cancer. In order to validate a specially created computed tomography device, a physical phantom is also created to be used for the purpose. Water was used to represent the glandular tissue, and polyethylene was used for the adipose tissue. The distribution of different anatomical structures in the breast is done by creating inserts in the model. The contrast substance – based on iodine and diluted to several different concentrations, is placed in rectangular chambers with dimensions of $4.5 \times 1.0 \times 1.0$ cm^3 (Huang et al., 2008).

A team of scientists from Italy developed an anthropomorphic phantom designed to test the diagnostic performance of dual-energy contrast-enhanced digital mammography imaging. The phantom is a parallelepiped made of plexiglass (polymethyl methacrylate – PMMA). PMMA spheres of different diameters are added to its wax-filled interior and a system of cavities that can be filled with different iodine concentrations (Contillo and Taibi, 2018).

CIRS Inc has made a prototype phantom for quality control in CESM with the following characteristics: the entire phantom is 55 mm thick, corresponding to the average thickness of a compressed breast. It consists of five parts – plates, each with a thickness of 10 mm. The top and the bottom plates have rounded edges and are made of adipose-equivalent material intended to mimic subcutaneous fat. Two other plates are made of material equivalent to adipose and glandular tissue, respectively. The base plate comprises material equivalent to 50% adipose tissue and 50% glandular tissue. This plate includes two groups of four 10 mm diameter cylinders made of the same base material to which an iodised component has been added. To obtain the overall appearance of the phantom, all plates must be stacked on top of each other, with the plate made of 100% glandular tissue equivalent positioned in the centre to mimic a glandular lesion (Figure 3.1), (R. Klausz, M. Rouxel, X. Mancardi, A.-K. Carton, 2018).

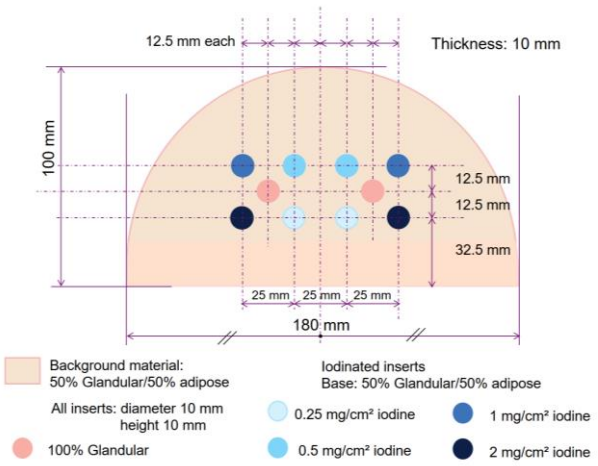

Figure 3.1. View of the plate with the iodine inserts

Copyright: figure 1 by (R. Klausz, M. Rouxel, X. Mancardi, A.-K. Carton, 2018)

Computational Models

In research, computational breast models save money and time. The following paragraph presents two of the most popular mathematical breast models (Bliznakova, 2020).

UPenn Anthropomorphic Breast Model

In 2002, a research group from the University of Pennsylvania presented their phantom – the first anthropomorphic computational breast model, created by modelling two ellipsoidal regions of large-scale tissue elements: mainly adipose tissue and fibroglandular tissue (Bakic et al., 2002-a) (Bakic et al., 2002-b). The fat compartments and the ductal distribution are both represented in these elements. The ducts are mathematically modelled by realistically distributed medium-scale phantom elements: shape, lobules and a simulated ductal tree. The ductal network model is implemented by branching matrices describing tree-like structure branching patterns (Bakic et al., 2003). The first software version of the phantom did not show sufficiently realistic results regarding Cooper's ligaments and fat tissue distribution. Therefore, a second version of the phantom was created. Figure 3.2 shows the comparison between two sections of the two versions of the UPenn software phantom.

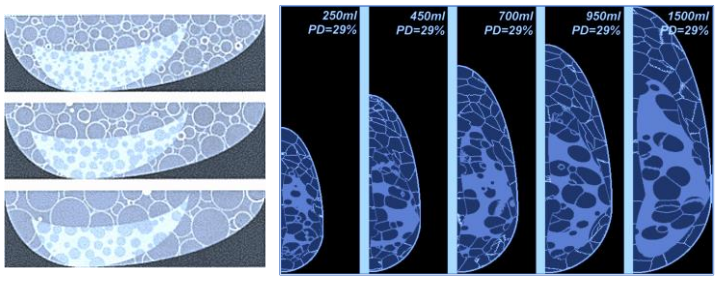

a b

Figure 3.2. Sections of the breast model with differently sized tissue elements: (a) 2002 software phantom (source: Bakic et al., 2002a); (b) 2011 software phantom (Bakic, Zhang and Maidment, 2011)

UPatras Anthropomorphic Breast Model

A research group at the University of Patras has developed an anthropomorphic breast model that represents a complex set of breast shape, ductal system, Cooper's ligaments, tissue structure and abnormalities, as shown in Figure 3.3 (Bliznakova et al., 2003). Creating a computational breast model always begins with modelling the external shape of the breast. This means determining the size and shape. The breast surface is modelled as a combination of two geometrical primitives: an elongated semi-ellipsoid and an elongated semi-hyperboloid. The duct system is simulated using a network of cylinders, probabilistically arranged in the breast as branches in a tree-like arrangement, starting from the nipple and restricted by the external breast contour. The mammographic texture simulates the presence of adipose, fibrous, connective tissues and other non-glandular tissue types that are not explicitly modelled. The Cooper's ligaments are modelled as a set of thin ellipsoid shells originating at randomly sampled positions in the breast model, while the pectoralis muscle is approximated as a cone-shaped object. Breast abnormalities are modelled with round, ovoid, elongated, and irregular shapes. Models of asymmetric breast abnormalities were created either by the "random walk" algorithm (Hintsala et al., 2009) or based on segmented patient data from breast CT (Bliznakova et al., 2019), (Dukov et al., 2019).

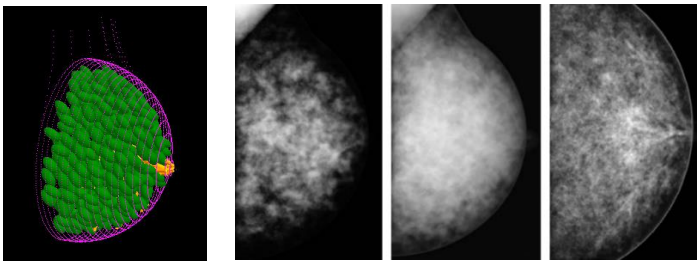

a b c d

Figure 3.3. Computational anthropomorphic breast model (a) and (b – d) simulated X-ray projections of mammary gland models

Copyright: Figure 5 – K. Bliznakova et al., 2010-a

In order to use these models in virtual examinations related to mammography and tomosynthesis, it is necessary to compress them, which is performed by a specially designed computational algorithm for compression (Zyganitidis, Bliznakova and Pallikarakis, 2007). The computational models and the

X-ray projections of these models are generated with the BreastSimulator application (Bliznakova et al., 2012), a special software application known to the scientific community, combining the functionalities mentioned above and being the primary tool of research and training related to x-ray images of the breast (Bliznakova, 2018). This application is used to generate anthropomorphic breast phantoms that have been successfully evaluated for use in breast CT optimisation (Mettivier et al., 2017), (Mettivier et al., 2016).

METHODS OF RESEARCH

Several software applications were used for the practical tasks of the thesis.

LUCMRFGen Software Application

LUCMFRGen is a software application that creates three-dimensional computational models of compressed breasts of different sizes and volumes (Figure 4.1), (Bliznakova, 2017).

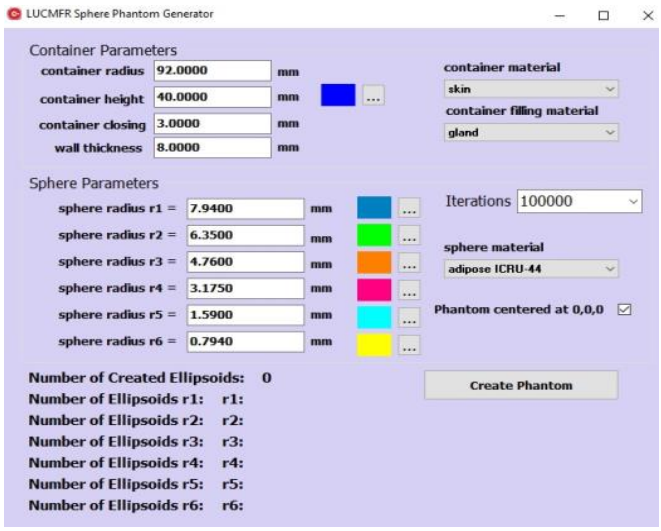

Figure 4.1. Screenshot of the LUCMFRGen software application during the process of breast creation

Breastsimulator Software Application

Using the BreastSimulator software application, a computational model of a compressed breast can be generated containing all the main components: shape; glandular and fibrous tissue, the milk duct system, Cooper's ligaments; pectoral muscles, blood vessels, skin; different formations (Figure 4.2), (K. Bliznakova et al., 2010b). All model details can be set with different values.

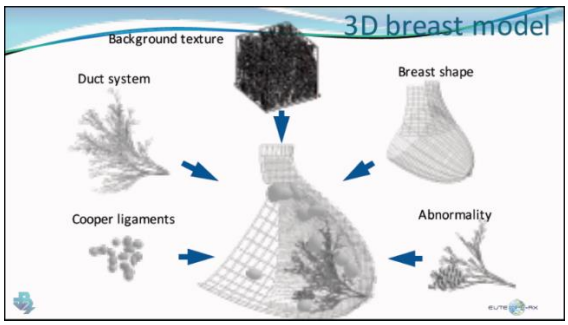

Figure 4.2. Computational breast modelling details

XRAYIimagingSimulator Software Application

It is a software application that can simulate 2D and 3D images (Figure 4.3, Figure 4.4).

Figure 4.3. A view from the XRAYIimagingSimulator for generating planar images in mammography and tomosynthesis

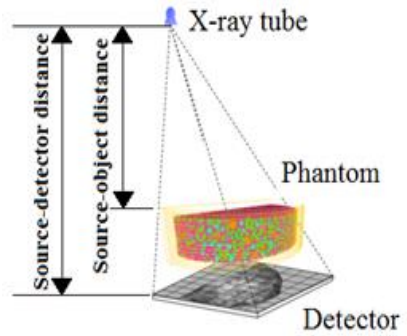

Figure 4.4. Simulated geometry during 2 D imaging

FDKR Software Application

The FDKR software application allows browsing projection images of different origins through stacks of reconstructed images of CBCT, CT and tomosynthesis (Figure 4.5), (Buliev, 2011).

The image reconstruction is based on the FDK algorithm (circular scanning trajectory), which assumes one-dimensional filtering of the projections using a high-pass filter with linearly increasing frequency response – the Ramp filter (Feldkamp, Davis and Kress, 1984).

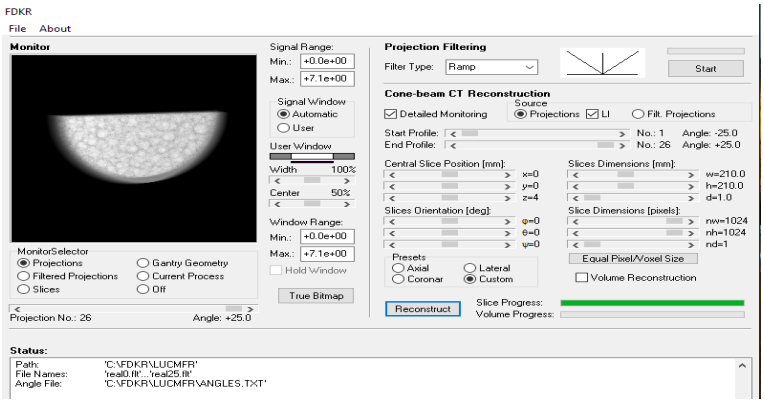

Figure 4.5. FDKR software application for image reconstruction

QualityPlatform Software Application

The QualityPlatform software application (Fig. 4.6) calculates a number of descriptors extracted from the X-ray images, such as fractal dimension, frequency analysis features, and first- and second-order statistics (Marinov et al., 2021). These descriptors can be extracted from patients and simulated mammographic images alike. The thesis uses four types of descriptors extracted from patients and simulated images with the software. Kurtosis measures the type of tail of the histogram distribution relative to the normal distribution of the results obtained. Skewness measures the skewness of the resulting histogram of the probability distribution of a real-valued random variable relative to its mean. Fractal image analysis correlates with the roughness of the investigated regions of interest, i.e. it is a parameter indicating a probable low or high risk of developing breast cancer (Marinov et al., 2021). The power spectrum is a measure of tissue structure or anatomical representation.

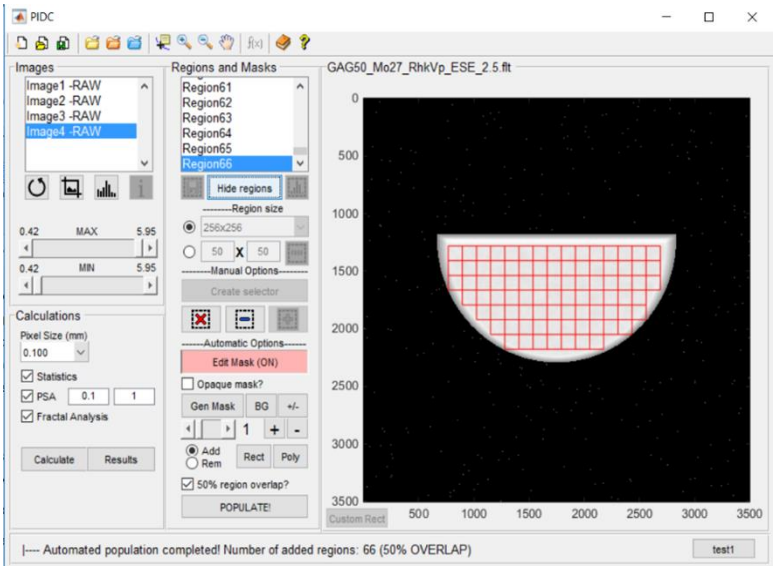

Figure 4.6. Screenshot of the QualityPlatform

EVALUATION OF A BREAST SOFTWARE MODEL FOR 2D AND 3D X-RAY IMAGING STUDIES OF THE BREAST

Introduction

Physical and computational phantoms are essential for developing, optimising, and evaluating modern x-ray imaging systems. It is crucial that both physical and software phantoms reproduce the breast anatomical characteristics as precisely as possible and are created in a way suitable for all steps of an actual breast examination. In most cases, physical breast phantoms are manufactured from a homogeneous mixture, which may result in a lack of realistic 2D and 3D image representation. While many research groups work on 3D anthropomorphic phantoms (Bakic *et al.*, 2002a),(Bakic *et al.*, 2002b), (Bakic *et al.*, 2003), (Bliznakova *et al.*, 2003), (Li *et al.*, 2009), (Lau *et al.*, 2012), (Carton *et al.*, 2011), (Kiarashi *et al.*, 2015), (Park *et al.*, 2010), (B. Chen *et al.*, 2011), (Pokrajac, Maidment and Bakic, 2012), there is not yet a consensus on a particular multi-purpose phantom. The degree of realism of the glandular structure is also variable, and inserting lesion-like objects remains a challenge.

In contrast to physical models, software models allow for precise, detailed modelling of the breast and its structures; they are more cost-efficient and different materials can be used for their creation. A physical breast phantom is presented by L Cockmartin et al. (Cockmartin, Marshall and Bosmans, 2012), which is based on the model of Gang et al. (Gang et al., 2010). It is used to compare conventional mammography and tomosynthesis to detect abnormal findings in the breast (Figure 5.1).

The purpose of this study is to (a) perform a detailed validation of the LUCMFRGen software application to generate compressed breast models similar to the physical model of Cockmartin et al. (Cockmartin, Marshall and Bosmans, 2012) and (b) to generate various compressed breast models composed of different materials and to compare their possible application in mammography and tomosynthesis.

Computational Models

The physical compressed breast phantom made by L Cockmartin et al. (Cockmartin, Marshall and Bosmans, 2012) is an acrylic semi-cylindrical container, 48 mm thick, 200 mm diameter corresponding to a 60 mm thick compressed breast (Cockmartin et al., 2017). Acrylic spheres with six different diameters: 15.88 mm, 12.70 mm, 9.52 mm, 6.35 mm, 3.18 mm and 1.85 mm, are inserted into the container. This physical phantom is a prototype designed to test and optimise planar mammography and three-dimensional tomosynthesis (Figure 5.1).

Figure 5.1. Picture of the physical breast phantom filled with water

Two physical models were created – one filled with air, and the other – with material whose properties are the same during x-ray irradiation as of a real breast (water). The images obtained from the physical phantom with water show similarity to images obtained from real mammography.

Four phantoms from different materials but with the same container dimensions were created for the purposes of this study (Table 5.1).

Table 5.1. Description of computational breast phantoms generated with the LUCMFRGen software tool

Phantoms	**Container**	**Filling material**	**Spheres**
Phantom1	PMMA	Air	PMMA
Phantom2	PMMA	Water	PMMA
Phantom3	Skin	Glandular tissue	Adipose
Phantom4	PMMA	Polyethylene	Water

The parameters used to obtain the computational breast models are: radius of the container – 92 mm, height – 40 mm, wall thickness – 8 mm, and small rubber ring for watertight closing – 3 mm. The spheres of the phantoms are described in Table 5.2.

Table 5.2. Description of the spheres contained in the phantoms

Radius of spheres	Number of spheres and volume in mm^3							
	Phantom 1		Phantom 2		Phantom 3		Phantom 4	
7.940	26	54515	26	54515	26	54515	26	54515
6.350	50	53626	50	53626	50	53626	50	53626
4.760	120	54211	120	54211	120	54211	120	54211
3.175	407	54565	407	54565	407	54565	407	54565
1.590	3242	54587	3242	54587	3242	54587	3242	54587
0.794	25822	54142	25602	53681	25493	53452	25510	53488

A screenshot of Phantom 1 is shown in Figure 5.2.

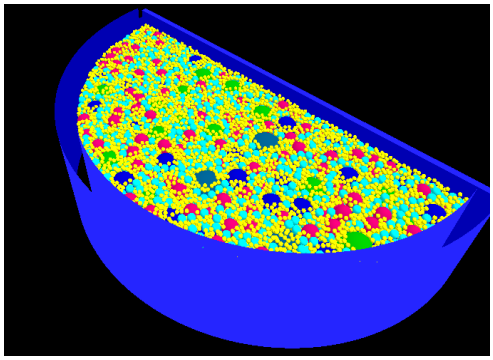

Figure 5.2. A computational model of a compressed breast was generated with the LUCMFRGen software tool

The phantoms differ in the material composition used for modelling the phantom parts: polymethyl methacrylate (PMMA), polyethylene, water, glandular and adipose tissue, skin and air..

Acquisition of Images from Physical Phantoms

The Siemens Mammomat Inspiration system (Erlangen, Germany) was used to produce projections with 2800 x 3518 pixels and a pixel pitch of 85μm (Fig. 5.3).

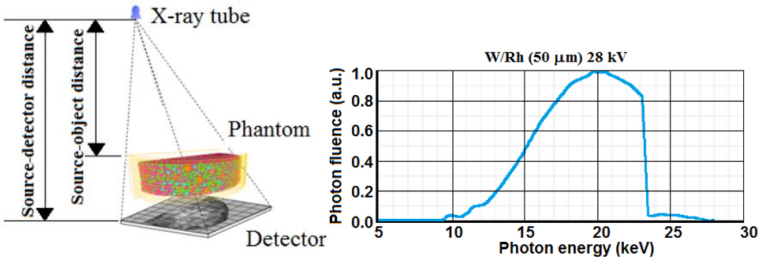

Figure 5.3. Image acquisition step: (a) simulated setup and (b) incident spectra beam

The distances between the radiation source and the breast compression panel and from the radiation source to the detector are 633 mm and 650 mm, respectively.

Planar x-ray projection images were obtained for an x-ray beam energy of 28 kVp and W/Rh as anode filter combination with the in-house developed *XRAYImagingSimulator*.

X-ray projection images are obtained with the simulation of x-ray photon transport through the phantom, based on the Bouguer-Lambert-Beer absorption law. Scatter radiation at this stage was not considered. The obtained scatter-free images were appropriately modified to include photon noise. For tomosynthesis simulations, the incident air kerma at the surface of the breast phantom was set to 7.4 mGy, while for planar mammography imaging, the incident air kerma was set to 4 mGy. The photon fluence was calculated as:

$$K = \left[\frac{\mu_{en}}{\rho}\right]_{air} \cdot E \cdot \Phi \qquad [5.1]$$

where K is the incident air kerma, E is the energy of the incident photons, Φ is the photon fluence, and $\left[\frac{\mu_{en}}{\rho}\right]_{air}$ is the mass energy absorption coefficients for air.

X-ray images of Phantom 1 and Phantom 2 were created using planar (craniocaudal) and tomosynthesis. Tomosynthesis was done with 25 projections (Sechopoulos, 2013a, 2013b).

Reconstruction of 3D Images

Tomosynthesis slices were reconstructed with the in-house image reconstruction tool FDKR (Buliev, 2011). For this study, three planes of interest, including the central slice, were reconstructed with a pixel size of 85 μm x 85 μm. Slice thickness was set at 1 mm. Images were reconstructed with both filtered back projection algorithms – a pure high-pass Ramp filter and a customised, smoother version of the Ramp filter.

Evaluation of Images

Images were evaluated using an in-house developed tool, *Quality Platform*, designed to extract image features. In this case, the pixel size was 85 μm, and the size of the regions of interest was 200 pixels x 200 pixels, resulting in 193 regions for which computation was performed (Figure 5.4).

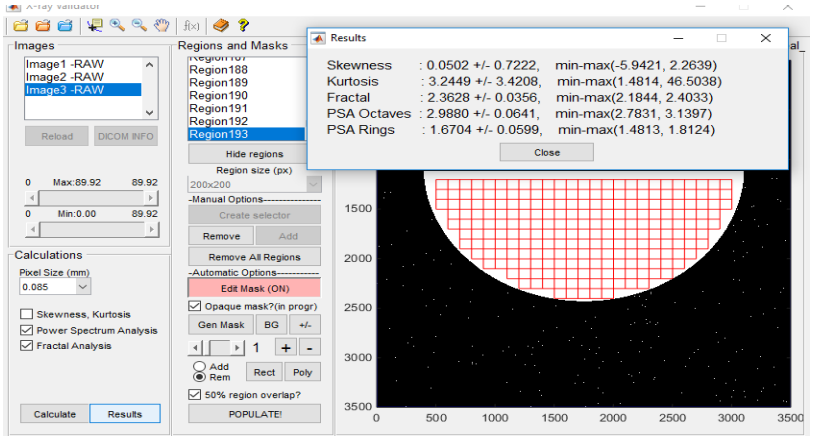

Figure 5.4. A screenshot from Quality Platform software's graphical user interface

Results

The validation of the obtained results includes a visual and quantitative comparison of the 2D and tomosynthesis real and simulated images for Phantom 1 and Phantom 2. The planar and reconstructed tomographic images of the other two computed tomography phantoms are also presented and quantitatively evaluated as a comparison with the previous ones.

Comparisons between Simulated and Experimental Planar Images

Comparisons between simulated and experimental planar images of phantom configurations 1 (PMMA spheres and air) and 2 (PMMA spheres and water) are shown in Fig. 5.5.

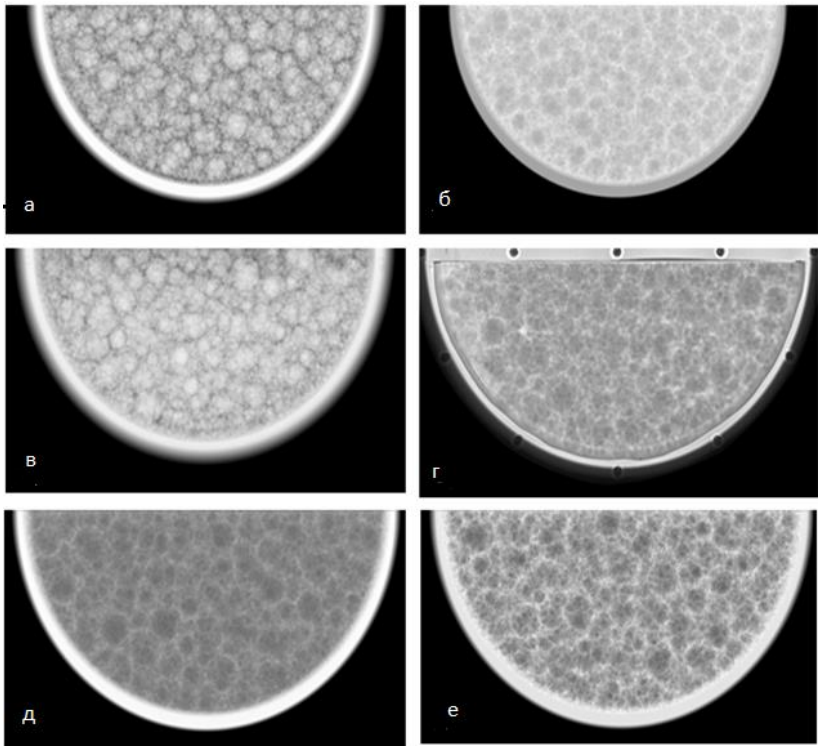

Figure 5.5. Comparison of simulated (first row) and experimentally acquired planar images (second row) of (a) Phantom 1 (PMMA with air) and (b) Phantom 2 (PMMA with water). Simulated mammography images of a breast phantom composed of adipose tissue (Phantom 3) and water (Phantom 4) spherical objects, shown in (e) and (f), respectively

The quantitative evaluation of simulated and experimental images is summarised in Table 5.4.

Table 5.4. Quantitative evaluation of simulated and experimental mammography images

Phantom	**Skewness**	**Kurtosis**	**Power law exponent (β)**	**Fractal dimension**
Phantom 1 (real)	0.72 ± 0.40	3.50 ± 1.26	3.23 ± 0.07	2.44 ± 0.02
Phantom 1 (sim)	0.04 ± 0.76	3.34 ± 3.99	3.38 ± 0.11	2.40 ± 0.01
Phantom 2 (real)	0.35 ± 0.54	3.13 ± 1.62	2.71 ± 0.15	2.08 ± 0.07
Phantom 2 (sim)	0.09 ± 0.71	3.26 ± 3.35	2.63 ± 0.11	2.10 ± 0.01
Phantom 3 (sim)	-0.30 ± 0.68	3.40 ± 3.56	2.40 ± 0.17	2.12 ± 0.01
Phantom 4 (sim)	-0.002 ± 0.93	3.65 ± 5.24	3.27 ± 0.01	2.08 ± 0.01

The images in Fig. 5.5-a-c are generated from phantoms filled with air, while images in Fig. 5.5-b-d are related to the phantoms with filling material water. Excellent conformity between simulated and experimentally acquired images is observed visually for both phantom configurations. This subjective conclusion is well supported by the good agreement between features extracted from experimental and simulated images. Figs 5.5-e-f show simulated planar images from phantoms 3 and 4, which

present an excellent visual appearance close to one produced from Phantom 2 (with the water filling material). A comparison of calculated parameters from images taken from Phantom 3 and Phantom 4 shows that the phantom with the characteristics close to the actual breast (Phantom 3) presents values close to Phantom 2 (PMMA – water). Also, the quantitative evaluation of Phantom 4 shows that a phantom with a design container based on PMMA, spheres made from polyethylene and filling material – water, is also a good candidate for such a physical breast phantom. The higher error values for kurtosis are due to the difference in the texture included in the regions used for the calculation.

Validation for Breast Tomosynthesis

Similarly to 2D mammography, a comparison between tomosynthesis images obtained from simulated and experimental projection images is shown in Fig.5.6

The side-by-side comparison of tomosynthesis images for phantom 1 (PMMA spheres and air, Fig. 5.6-a-c) and phantom 2 (PMMA spheres and water, Fig. 5.6-b-d) shows an excellent visual agreement between simulated and experimental tomograms. The observed blurring in the images is expected, and it is mainly due to (1) the limited scanning arc in the projection acquisition for the tomosynthesis and (2) due to the conical profile of the x-ray beam (the filtered back-projection algorithm assumes that the detector rows acquire images from x-rays lying in a plane but away from the source trajectory plane, that is not valid anymore). The visual comparison identifies the similar appearance of simulated structures in the computational and physical phantoms. Logically, experimentally obtained tomograms appear more blurred compared to simulated. This is due to the fact that x-rays were not simulated within the detector.

Quantitatively, the evaluated features of the tomosynthesis images are shown in Table 5.6

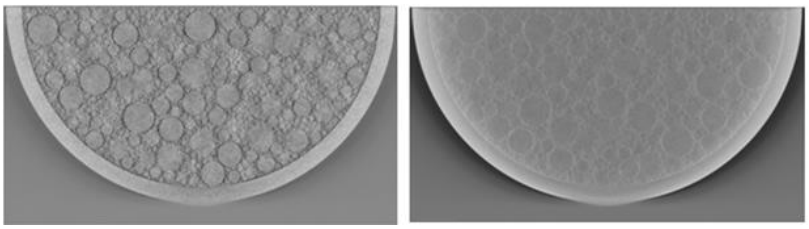

a b

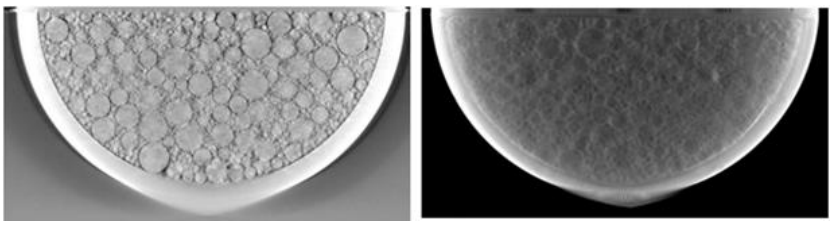

c d

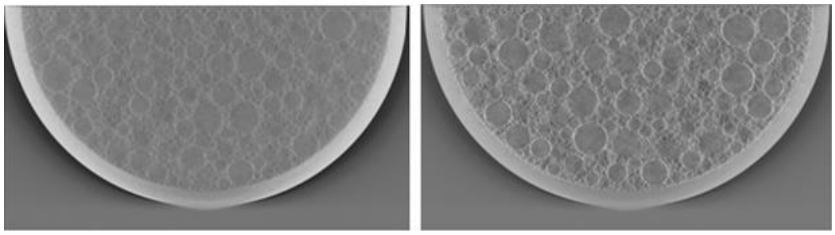

e f

Figure 5.6. Comparison of reconstructed images from simulated (first row) and experimentally acquired planar images (second row) of (a) Phantom 1 (PMMA phantom filled with air) and (b) Phantom 2 (PMMA filled with water). For comparison purposes, simulated mammography images of a breast phantom composed of (e) Phantom 3 – skin, and (f) Phantom 4 (polyethylene spheres)

Table 5.5. Quantitative evaluation of 3D simulated and experimental images

Phantom	**Skewness**	**Kurtosis**	**Power law exponent (β)**	**Fractal dimension**
Phantom 1 (real)	-0.70 ± 0.60	3.88 ± 2.09	3.04 ± 0.11	2.57 ± 0.04
Phantom 1 (sim)	-0.30 ± 0.51	3.95 ± 0.57	2.81 ± 0.06	2.21 ± 0.01
Phantom 2 (real)	0.07 ± 0.47	3.35 ± 2.04	1.90 ± 0.19	3.21 ± 0.05
Phantom 2 (sim)	-0.02 ± 0.38	3.14 ± 2.06	1.35 ± 0.19	2.56 ± 0.02
Phantom 3 (sim)	1.00 ± 0.48	3.89 ± 0.97	1.59 ± 0.03	2.51 ± 0.01
Phantom 4 (sim)	1.64 ± 0.95	6.66 ± 4.11	2.01 ± 0.05	2.47 ± 0.01

A comparison of β between 2D and tomosynthesis slices (Tables 5.4 and 5.5) shows lower β values for 2D images. This is also reported in other publications concerning actual and simulated data (Cockmartin *et al.*, 2014), (Cockmartin, Bosmans and Marshall, 2013). The 2D mammography fractal analysis results show an excellent correlation between simulated and experimentally obtained results. This is due to the large photon fluence used to form one planar image mammography and the negligible differences between simulated and experimental results for fractal dimensions. Conversely, due to the 25 images acquired during tomosynthesis with a total incident exposure equal to that for the 2D image, the photon fluence per projection image decreases, resulting in more noise and, therefore, a higher fractal dimension. Besides this, there are also other noise sources in the detector (not presently simulated), leading to higher values for the fractal dimension. The almost ideal

properties of our detector resulted in less noise and, therefore, lower values for the fractal dimension. Finally, skewness and kurtosis correlate well for 2D and tomosynthesis images.

This study's results were compared to those demonstrated by the UPenn software breast phantom (Bakic P.R., Carton Ann-Katherine, Reiser I., Maidment A.D.A., 2010). The β values for Phantom 2, which closely resemble the actual mammography texture properties, are similar to those reported by Bakic et al. (Bakic P.R., Carton Ann-Katherine, Reiser I., Maidment A.D.A., 2010) for the evaluation of the UPenn software phantom. The authors report an average β value of 2.65 (1.325 to be consistent with our presentation method) for 450 ml phantoms and 2.62 (corresponding to 1.31 for our case) for 1500 ml phantoms. Similar to this study, the authors did not include any quantum or detector noise and have not included scatter or detector blur.

In the case of 3D imaging, lower values for ß are computed for simulated tomograms compared to real ones. This may be attributed to the already mentioned fact that x-rays were not simulated in the detector.

The evaluation suggests that the software phantom and the acquisition geometry are modelled in sufficient detail to receive a similar visual appearance. Efforts are focused on the simulation of x-ray imaging by using the Monte Carlo techniques to represent precisely the scattering events and improve the shape of the beads.

Since the number of generated spheres is about 29 000, using the Monte Carlo technique may not be the best choice for simulating the X-ray process since it can only simulate serial events (K Bliznakova et al., 2010). Simulations reported in the literature concern computational phantoms composed of a much smaller number of objects. Our phantom needs to be converted in order to use the Monte Carlo technique, which is already planned as the next step.

Once validated, this software tool may be used to design and evaluate more complex images. Testing and evaluating different scenarios for this imaging technique saves time and is cost-effective, especially before real practical work. In silico results may be helpful to optimise planned experimental work and imaging setups prior to performing the practical work.

Conclusions

This paper presents the evaluation of a computational breast phantom, which closely mimics the structure (shape, dimensions and content) and x-ray imaging characteristics of the corresponding real physical breast phantom. The subjective and the quantitative comparison showed a good correlation between actual and simulated planar and tomographic images from the phantoms. Moreover, the additional virtual experiments with spheres simulated from adipose (Phantom 3) and polyethylene

(Phantom 4) showed that quantitatively and visually, the images from these phantoms are close to those generated from Phantom 2 – where the filling material was water. The computed values for the β parameter and the fractal dimension in the case of 3D imaging are higher, but the detector characteristics were not simulated while they should be. This is not a straightforward task and has been planned as part of our future work. The software platform application is designated for developing and evaluating a more realistic physical breast phantom intended for advanced breast imaging techniques.

INFLUENCE OF INCIDENT MAMMOGRAPHY SPECTRA AND PHANTOM BREAST CHARACTERISTICS ON MAMMOGRAPHY IMAGE FEATURES

Introduction

Breast cancer is a disease which is curable if detected on time. The density of the breast is essential for the quality of the image parameter of the imaging system because dense tissue can hide cancer. The presence of dense breast tissue lowers the sensitivity of mammography (Schulz-Wendtland *et al.*, 2009), (AL Mousa *et al.*, 2014). For thicker and/or denser breasts, a higher-energy x-ray beam is needed to achieve adequate tissue penetration (American College of Radiology, 2017). Therefore, optimisation of all mammography units is essential for the early detection of breast cancer. In this task, the availability of breast phantoms is a requirement. Clinical investigations might be expensive and time-consuming; software phantoms instead are a better alternative. Computer models mimic the anatomy and shape of the female breast and are used in the simulation of x-ray imaging and the generation of x-ray projection (Bliznakova, 2020).

This study aims to generate different thickness and content breast phantoms and their synthetic mammograms using a designated x-ray software simulator and to evaluate the effect of incident mammography spectra and phantom breast characteristics on the extracted mammography imaging features.

Phantoms

Using the phantom created by L Cockmartin et al., which has already been validated, and using the LCMFRGen software platform, four computer phantoms were created with different thicknesses and compositions (Table 6.1).

Four phantoms with different thicknesses and compositions were generated. The first phantom – **Phantom 1,** consists of a container filling material made from the gland, while the sphere's material is adipose. Two phantoms are designed with the same material composition but different thicknesses: 50 mm and 60 mm. The algorithm for the sphere's generation implements the sphere packing concept

for unequal non-overlapping spheres in container space. The diameters of the spheres are: 7.94 mm, 6.35 mm, 4.76 mm, 3.175 mm, 1.59 mm and 0.79 mm. The number of the created ellipsoids is 37 854 for the phantom with a thickness of 50 mm and 44 926 for the phantom with a container height of 60 mm. The container and the spheres of **Phantom 2** are simulated from gland tissue, while the container filling material is adipose tissue. Again, two computational phantoms are generated. The number of the created ellipsoids is 37 534 for the phantom with a thickness of 50 mm and 45 425 for the phantom with a container height of 60 mm.

Table 6.1. Description of the computational breast phantoms generated with the LUCMFRGen software tool used in the study

Phantoms	**Container**	**Spheres**	**Filling material**	**Container height**	**Number of spheres**	**Density by volume, %**	**Density by mass, %**
Phantom 1	Gland	Adipose	Gland	50	37854	36%	38%
	Gland	Adipose	Gland	60	44926	36%	38%
Phantom 2	Gland	Gland	Adipose	50	37534	64%	65%
	Gland	Gland	Adipose	60	45425	64%	65%

Phantom 1 is shown in Figure 6.1. The densities of the created breast models were calculated using the following equations:

$$Breast\ Density\ by\ volume, \% = \frac{\text{Volume of the gland}, cm^3}{\text{Volume of gland+Volume of adipose}, cm^3} * 100 \quad [6.1]$$

$$Breast\ Density\ by\ mass, \% = \frac{\text{Mass of the gland,g}}{\text{Mass of gland+Mass of adipose}} * 100 \quad [6.2]$$

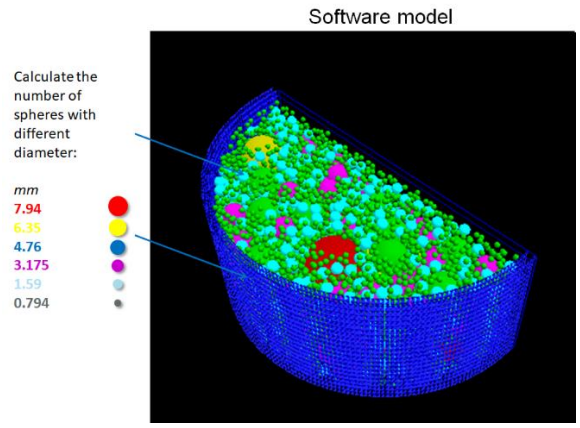

Figure 6.1. Phantom 1 preview

Generation of Projection Images

XRAYImagingSimulator – an in-house software tool, is used to create the planar x-ray projection images. In the present study, the module for analytical x-ray image formation is used, as simulated mammography images are obtained for source-to-isocenter, and source-to-detector distances are 600 mm, and 660 mm, respectively. The detector resolution is 10 pixels/mm, while the image size is 3500 x 3500 pixels.

For the generation of the images, eight mammography x-ray spectra are modelled and shown in Fig.6. 2: Mo 25, Mo/Rh 27, Mo 27, Mo/Rh 28, Mo 30, Rh/Rh 29, Rh 30, Rh/Rh 31. For this purpose, a Matlab computational code was developed to obtain these spectra, and each phantom was irradiated with each spectrum.

Simulated x-ray spectra and their average energies are shown in Table 6.2.

Table 6.2. Simulated x-ray spectra and their mean energies

Spectrum	Mo/Mo 25 kVp	Mo/Rh 27 kVp	Mo/Mo 27 kVp	Mo/Rh 28 kVp	Mo/Mo 3 0 kVp	Rh/Rh 29 kVp	Rh/ Rh 30 kVp	Rh/Rh 3 1 kVp
EkV	15.95	16.2	16.37	16.41	16.93	18.28	18.52	18.75

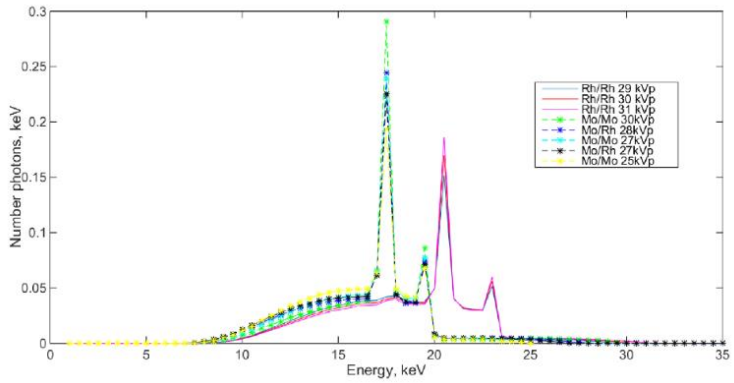

Fig.6.1. Modelled x-ray mammography spectra used in the study

Photon noise is added to each projection for different ESE (Entrance surface exposure) 2.5 mGy, 3 mGy and 3.4 mGy. Calculations of features from the simulated phantoms were performed using the Quality platform.

Results and Discussion

Simulated x-ray images of the generated projection images of the phantoms with the same thickness but different elemental compositions are shown in Fig. 6.3.

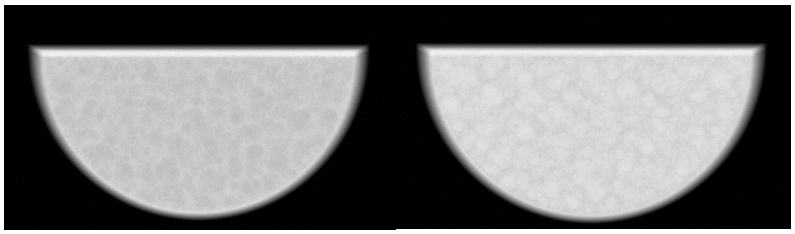

a b

Fig. 6.3. Simulated x-ray images of: (a) phantom GAG50 and (b) Phantom GGA50 with Mo25kVp

Influence of Phantom Materials

Results of the studied parameters from the presentation of the different types of material used for modelling the computational breast phantoms are shown in Figure 6.4 for the phantom thickness of 50 mm and in Figure 6.5 for the phantom thickness of 60 mm.

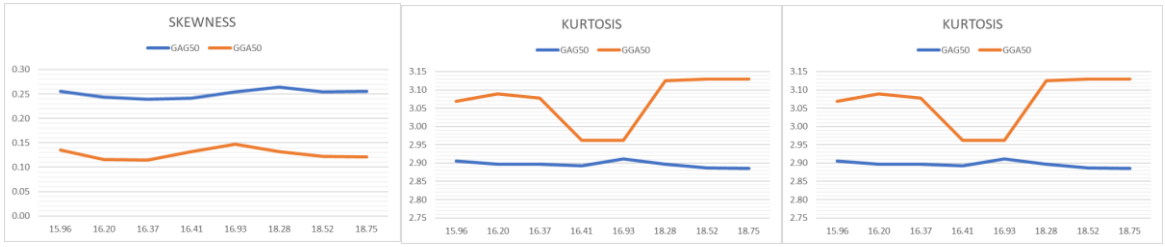

a b c

Figure 6.4. Comparison of the main features extracted from simulated mammographic images from GAG phantom and 50 mm thick GGA: (a) skewness, (b) kurtosis, and (c) fractal analysis. Values on the x-axis indicate the average energy of the mammographic spectra in keV

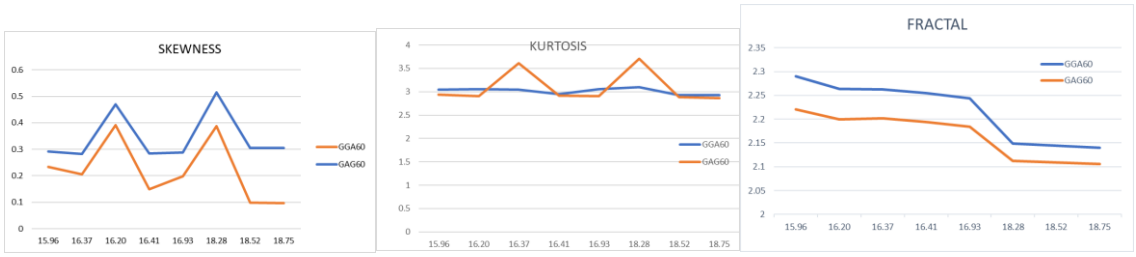

a b c

Figure 6.5. Comparison of the main features extracted from simulated mammographic images from GAG phantom and 60 mm thick GGA: (a) skewness, (b) kurtosis, and (c) fractal analysis

For the same phantom thickness:

- *Skewness* has higher values for GAG (a gland for the container filling material, adipose for the spheres) compared with GGA (gland for the container material and the spheres, and adipose for the container filling material). This suggests that the GGA combination represents a denser breast than GAG because a dense breast would have lower skewness values (Li *et al.*, 2005).
- *Kurtosis* is higher for the GGA50 phantom (gland for the container material and the spheres, and adipose for the container filling material) than GAG50 (a gland for the container and the container filling material, adipose for the spheres). The kurtosis value is higher in the phantom combination GAG 60 than the result from phantom combination GGA60 just for the energies 16.37 kV and 18.28 kV.
- *Fractal dimension* is higher for GGA, the phantom with both thicknesses of 50 mm and 60 mm, compared to the phantom GAG with thicknesses of 50 mm and 60 mm.

Influence of Phantom Thickness

Fig. 6.6 summarises the influence of phantom thickness on the extracted mammographic features for the GGA phantom and the different incident spectra.

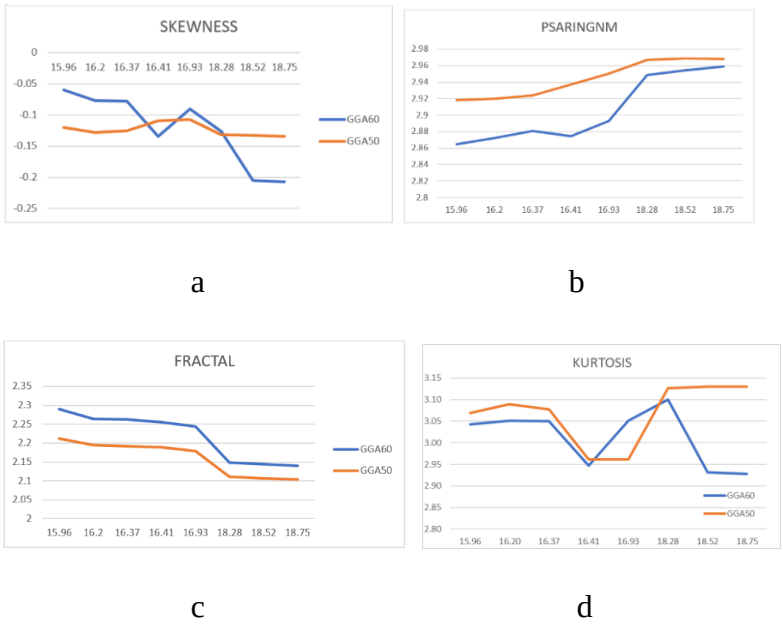

Fig. 2.6. The influence of the phantom thickness on the extracted features for GGA for the different incident spectra. The values on the x-axis show the mean energy of the mammography spectra in keV

The skewness values are higher for the phantom with the higher thickness for lower mammographic incident energies, while the kurtosis values are opposite compared to the skewness.

The phantom with higher thickness shows a higher value for the fractal dimensions. Similarly, the higher the phantom thickness is, the higher β factors from the power law spectra are obtained.

For both phantoms – GAG and GGA, the values of the fractal dimensions decrease with the increase of incident mammography energy, while the β factor from the power law spectra increases with the increase of the incident mammography energies.

Conclusions

Fractal dimension depends on the incident x-ray spectra, while kurtosis and skewness are almost constant statistical features. Increasing the mean energy of the mammography spectra results in lower fractal values and higher β factors from the power law spectra. The comparison between the two basic phantoms (GGA and GAG) reveals which material combination might represent a denser breast, i.e. GGA, while the GAG phantom represents a fatty breast. The gene-mutation carriers tend to have denser breast tissue than those in low-risk women. These features may be used as basic parameters in the design of software applications for breast density evaluation. Currently, the results from more

than twenty radiographic features extracted from the images are under evaluation. They will be used in designing a deep learning system to classify mammographic breast density.

COMPUTATIONAL BREAST MODELS FOR CONTRAST-ENHANCED SPECTRAL MAMMOGRAPHY

Introduction

The overlap of diagnostic relevant tissue structures in women with dense breasts and limitations of the applied dose due to the radiation susceptibility of the breast are some of the main issues in breast imaging (Heck *et al.*, 2019). New technology for early detection of breast cancer is the Contrast-Enhanced Spectral Mammography (CESM), a novel technique based on dual-energy acquisitions after injection of an iodine-based contrast agent. Two x-ray images are obtained at two different x-ray energies concerning the K-edge of the contrast inserted material, and hypervascularised breast lesions are expected to be seen on the recombined images (Carton AK, Saab-Puong S, 2012)

Some authors suggest that intensity and pattern of enhancement on CESM might bring (together with the results of diagnostic imaging methods) not only the confirmation of the presence or absence of a tumour but also prognostic information (Mohamed Kamal et al., 2015), (Luczynska et al., 2018). The design, optimisation and validation of physical phantoms customised to specific radiological tasks require both materials and time. Phantoms and, more specifically, computational phantoms may be of assistance in exploring and testing novel ideas before developing the physical phantom with established from the simulations' optimised parameters. This study aims to design different in complexity computational CESM phantoms, to objectively and subjectively investigate the visibility of iodine inserts in the CESM images and determine which is appropriate for physical manufacturing.

Phantoms' Design with Contrast Agents

Three computational phantoms were designed with the in-house developed software tools *XRAYImagingSimulator* и *LUCMFRGen*.

PMMA is used to create all phantoms, and six cylinders modelled with Omnipaque are inserted in each. The first phantom (Figure 7.1-a) has a parallelepiped shape, with base dimensions of 203 mm x 152 mm and a thickness of 25.4 mm. The inserted cylinders have a radius of 9.5 mm and a height varying from 0.5 mm to 20 mm. The second phantom (Figure 7.1-b) has a semi-cylindrical shape, with a radius of 50 mm and a height of 45 mm. The radius of the inserted cylinders is 10 mm, and the height varies – 2 mm, 3 mm, 4 mm, 5 mm, 6 mm, and 8 mm. The third phantom was designed as a

heterogeneous breast phantom (Figure 7.1-c). It has the shape of a semi-cylinder with a radius of 50 mm and a height of 48 mm. The radius of the inserted cylinders is 8 mm, and the height is from 0.1 mm to 0.6 mm. Heterogeneity is achieved by creating a heterogeneous background using more than 8 000 spheres of different diameters, which vary between 0.79 mm and 7.94 mm**.**

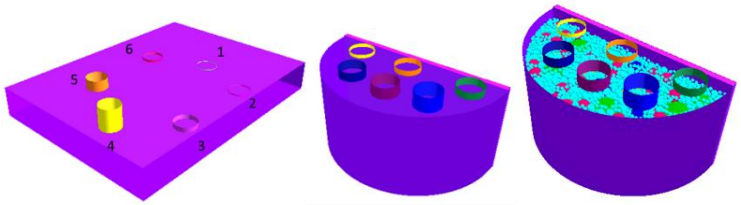

a b c

Figure 7.1. Generated computational models of a compressed breast: a) Phantom 1, b) Phantom 2, c) Phantom 3

Generating Planar Images and CESM Images Acquisition

For each phantom, two simulated radiographs were computationally generated: one at energy 20 keV and one at a higher energy – 34 keV. Energies were selected respectively below and above the iodine K-edge, which is at 32.17 keV. The images were processed to create a resulting image, called a recombined CESM image, that visually intensifies the contrast by suppressing the surrounding background tissue. These images were synthesised with the second module of the *XRAYImagingSimulator*. The modelled geometry is shown in **Грешка! Източникът на препратката не е намерен.**, where the x-ray tube and detector were modelled at a distance D1 and D2 equal to 603 mm and 660 mm, respectively.

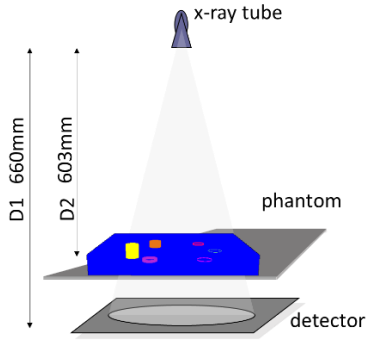

Figure 7.2. Simulated x-ray imaging geometry synthesises x-ray images from the computational CESM phantoms

The simulated x-ray projection images of the computational phantoms were modelled with a pixel size of 100 μm. Modelling of detector noise was not tasked in this simulation study. The final intensity images are based on Beer's law:

$$I = I_0 * \exp\left(- \int_{ll} \mu(x, y, z) dl \right)$$

[7.1]

where μ(x,y,z) is the spatially dependent linear attenuation coefficient, l is the path length through the object, and I_0 is the radiation intensity of the source assumed to be the same for all angles.

This concept of using two different energies is exploited to obtain better visualisation for specific tissues. X-ray images are acquired at different diagnostics x-ray energies. Subsequently, these primary images are processed by using weighted subtraction, which results in the removal of a given tissue type in the recombined image (Jacobson, 1953). In this study, the low and high-energy images are subtracted in order to remove the phantoms' background and increase the visibility of iodine inserts.

Evaluation

The evaluation of the designed computational phantoms was implemented subjectively by assessing the visibility of the inserts in the recombined images and, objectively, by calculating the subject contrast of these inserts.

For this purpose, two types of regions of interest (ROI) were assigned for each simulated low energy and recombined image. Expressly, the first type of ROIs is referred to as ROI_{object} and is positioned within the areas of the contrast agent insert, while the second type of ROI is referred to as ROI_{back} and is positioned in the background area. All ROI were 60 pixels x 60 pixels, corresponding to an area of 36 mm^2. The average values of the pairing ROIs were taken for further calculations as follows:

$$C = \frac{R_{object} - R_{back}}{R_{back}}$$

[7.3]

Results

Simulated planar projections of computer Phantom 1 for energies 20 keV and 34 keV are shown in Figures 7.4-a-b, while Figure 7.4-c shows the image obtained after weight subtraction.

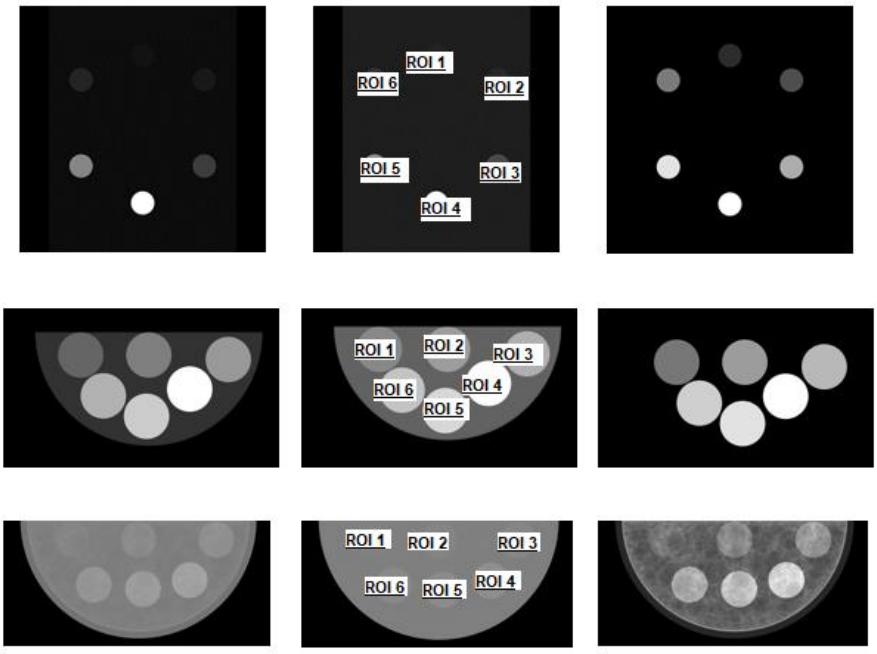

a b c

Figure 7.4. Pictures of the projections of Phantom 2: a) with energy 20 keV, b) with energy 34 keV, c) the recombined image

Table 7.4 summarises the contrast calculations for the three computational phantoms.

Table 7.4. Objects'contrast evaluation

	ROI1	ROI2	ROI3	ROI4	ROI5	ROI6
Phantom 1 contrast at 20 keV	0.47	0.95	3.79	18.93	9.47	1.89
Phantom 1 recombined contrast	60.50	120.99	483.97	2419.87	1209.94	241.99
Phantom 2 contrast at 20 keV	1.023	1.54	2.05	4.09	3.07	2.56
Phantom 2 recombined contrast	130.64	195.96	261.28	522.56	391.92	326.60
Phantom 3 contrast at 20 keV	0.04	0.09	0.14	0.27	0.22	0.17
Phantom 3 recombined contrast	0.69	0.48	0.65	1.28	0.99	0.79

The improvement in contrast in the CESM image compared to the low-energy image is shown in Figure 7.5.

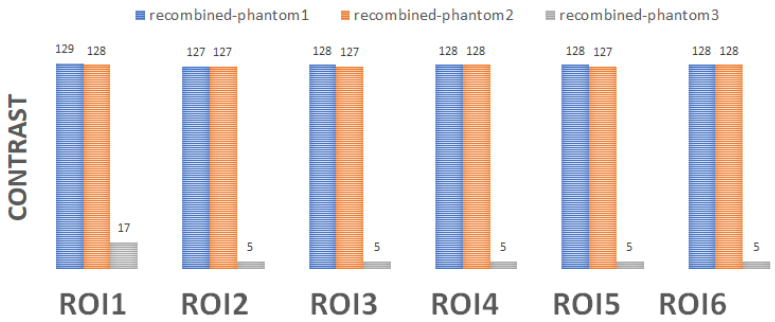

Figure 7.5. The contrast in the different ROIs for the recombined phantoms images improved

Discussion

The contrast inserts in the first phantom are cylinders with varying heights (from 0.5 mm to 20 mm) and a constant diameter of 19 mm. These cylinders are filled with Omnipaque used in diagnostics procedures where contrast enhancement is required. The visual comparison of objects between the recombined and low-energy image (Figure 7.4, first row) shows that the visibility of cylinders with higher thickness increases; however, the visibility of the thinner objects is also well improved. As seen in **Грешка! Източникът на препратката не е намерен.**-a (first row), the cylinder that is 0.5 mm thick (ROI 1 of the simulated low x-ray energy image) is barely noticeable, but this Omnipaque object is well visible in the recombined CESM image **(**Грешка! Източникът на препратката не е намерен.-c, first row). This result is also well supported by the objective evaluation of the contrast in low-energy and recombined images, showing an approximately 129-fold amplification of the contrast values for the contrast-enhanced image (**Грешка! Източникът на препратката не е намерен.**). The same contrast improvement is also visible for the remaining iodine cylinders. This is due to the fact that this phantom is characterised by a homogeneous background, i.e., the PMMA parallelepiped, which influence was subtracted as a result of the subtraction algorithm.

The second phantom represents a breast in a compressed form (Грешка! Източникът на препратката не е намерен.-c, second row). Visually, the contrast of all contrast inserts is exceptionally well enhanced in the CESM image due to both the subtraction algorithm and the relatively large, simulated area of the objects (20 mm in diameter). Similarly, the objective evaluation in Грешка! Източникът на препратката не е намерен. showed approximately a 127-fold improvement of the object contrast, valid for all contrast objects, due to the homogeneous phantom's background.

Finally, the third phantom is characterised by a highly heterogeneous background (Figure 7.4, third row), which is due to the x-ray projections consisting of a large number (more than 8 000) of various in diameter PMMA spheres placed in water, thus creating a realistic mammography background (Baneva et al., 2017), (Cockmartin, L., 2016). The enhancement in the objects' contrast in the recombined CESM image is visible for all contrast objects. The most remarkable contrast improvement in the recombined CESM image (**Грешка! Източникът на препратката не е намерен.**-c, third row) is observed for the projected cylinder with a thickness of 0.1 mm. Although the visual enhancement of the recombined image of the heterogeneous phantom is not relatively high compared to the second homogeneous phantom, shown in **Грешка! Източникът на препратката не е намерен.**, second row, there is still an enhancement for the thinner (0.1 mm) object.

Overall, the results show that for all computer-generated phantoms, the contrast of the objects under investigation (the ROI) is higher than the contrast for the low-energy image. The developed phantoms could also be used in studying the correlation between quantitative assessment of contrast enhancement in CESM image and histopathology (Rudnicki et al., 2019), which study would be feasible due to the developed by the researchers at the Medical University of Varna database of breast cancer cases (Bliznakova et al., 2019).

Of the studied phantoms, the Phantom 3, characterised by a heterogeneous background, was demonstrated to produce realistic x-ray projection images and the appearance of contrast inserts. This phantom is planned to be manufactured for validation and further application in contrast-enhanced x-ray imaging applications. Further work also concerns the possibility of adding specific detector noise to the simulated ideal x-ray images, which will contribute to the realism of the images.

Conclusion

Improvement of the image quality of contrast inserts compared to low-energy x-ray images of the computational phantoms is detected for all three phantoms. The simulations with the complex computational model revealed that the heterogeneous background had been successively depressed while improving the visibility of the iodine inserts. The heterogeneous breast phantom might be used as a reference tool for information about the needed iodine concentration, which needs to be applied during the procedure to obtain significant enhancement in the suspicious area. Current work includes the construction of the physical breast phantoms and their thorough evaluation.

CONCLUSION

This paper presents the evaluation of a computational breast phantom, generated with *the LUCMFRGen platform*, which closely mimics the structure (shape, dimensions and content) and x-ray imaging characteristics of the corresponding real physical breast phantom. The subjective and the quantitative comparison showed a good correlation between actual and simulated planar and tomographic images from the phantoms. For this reason, the application of the software platform is intended for the development and evaluation of a more realistic physical breast phantom customised for advanced breast imaging techniques. Efforts are focused on the simulation of x-ray imaging by using the Monte Carlo techniques to represent precisely the scattering events and improve the shape of the spheres. Our phantom needs to be converted to be suitable for the Monte Carlo technique, which is planned as the next step.

Once validated, this software tool may be used to design and evaluate more complex images. Testing and evaluating different scenarios for this imaging technique saves time and is cost-effective, especially before real practical work. In-silico results may be helpful to optimise planned experimental work and imaging setups prior to performing the practical work.
The results of the studied parameters from the presentation of the different types of material used for modelling the computational breast phantoms showed that the two basic phantoms (GGA and GAG) reveal which material combination might be used for the representation of a denser breast, i.e. GGA, while GAG phantom represents fatty breast. The gene-mutation carriers tend to have denser breast tissue than those in low-risk women. These features may be used as basic parameters in the design of software applications for breast density evaluation. Currently, the results from more than twenty radiographic features extracted from the images are under evaluation. They will be used in designing a deep learning system to classify mammographic breast density.

The results from the created computational breast phantoms for CESM revealed that the developed phantoms could be used in studying the correlation between quantitative assessment of contrast enhancement in CESM images and histopathology. Such a study is feasible due to the developed by the researchers at the Medical University of Varna database of breast cancer cases. Of the studied phantoms, Phantom 3 – characterised by heterogeneous background- produced realistic x-ray projection images and the appearance of contrast inserts. This phantom is planned to be manufactured for validation and further usage in contrast-enhanced x-ray imaging applications. Further work also concerns the possibility of adding specific detector noise to the simulated ideal x-ray images, which will contribute to the realism of the images.

THESIS CONTRIBUTIONS

- A methodology was developed to create different by content computational breast models.
- Four complex and innovative computational breast models with different inhomogeneous content were created.
- X-ray images of two of these 4 computational phantoms were modelled using two methods – planar mammography and tomosynthesis.
- Both back projection algorithms were used – pure high-frequency Ramp filter and its personalised version- to reconstruct the images.
- A quantitative assessment of the simulated and experimental mammographic images from the created computational breast models is presented.
- The 3D images obtained from simulated and experimental projection images were compared.
- Successful validation of the LUCMFRGen software tool for applications in mammography and tomosynthesis was performed.

Regarding the assessment of the effect of the incident radiation spectrum and its influence on the phantom:

- Four innovative computational phantoms of a compressed breast with different thicknesses and compositions were created.
- A Matlab script was developed for modelling eight energy mammographic spectra - Mo 25, Mo / Rh 27, Mo 27, Mo / Rh 28, Mo 30, Rh / Rh 29, Rh 30, Rh / Rh 31 to generate the images.
- Simulated X-ray images of each phantom were obtained for all input spectra.
- Results from the different types of materials and different energy spectra used for modelling the breast phantoms were studied and compared.
- A methodology was developed to study the influence of the thickness of the compressed breast as a function of the different energies of the ionising radiation.
- A methodology for extracting descriptors from X-ray images was developed.
- A correlation between the fractal index and the β factor as a function of the incident radiation was established.

Regarding the creation of a physical phantom for the purposes of CESM:

- Three (3) computational breast models have been modelled for the purposes of CESM, which will be used for the development of physical ones.
- A methodology for modelling CESM has been developed.

- The difference between phantoms with a homogeneous and inhomogeneous texture was demonstrated by introducing the contrast parameter for image comparison.

PUBLICATIONS

P1. Design and use of computational models for contrast-enhanced spectral mammography, Scripta Scientifica Medica, 2022 | journal-article, https://journals.mu-varna.bg/index.php/ssm/article/view/8361

P2. A METHOD FOR MODELING OF CONTRAST ENHANCED MAMMOGRAPHY IMAGING: A SIMULATION STUDY, Bulgarian journal of public health, 2022-03 | journal-article

P3. Influence of Incident Mammography Spectra and Breast Phantom Characteristics on Mammography Features, Contemporary Methods in Bioinformatics and Biomedicine and Their Applications, 2022 | book-chapter, DOI: 10.1007/978-3-030-96638-6

P4. COMPUTATIONAL BREAST MODELS DEDICATED TO CONTRAST ENHANCED SPECTRAL MAMMOGRAPHY, RAD 2021, 2021 | conference-abstract

P5. Investigation of models for breast contrast-enhanced mammography: simulation results, NMPEC-2020, 2020-11 | conference-abstract

P6. Evaluation of a breast software model for 2D and 3D X-ray imaging studies of the breast, Physica Medica, 2017 | journal-article, DOI: 10.1016/j.ejmp.2017.04.024EID: 2-s2.0-85018784888Part of ISSN: 1724191X 11201797

Conferences:

C1. Ninth international conference on radiation in various fields of research, June 14-18, 2021, Montenegro

C2. International Symposium on Bioinformatics and Biomedicine, October 8-10, 2020, Burgas, Bulgaria.

C3. XIII-TH NATIONAL MEDICAL PHYSICS AND BIOMEDICAL ENGINEERING CONFERENCE: 2-13 NOVEMBER 2020, PLOVDIV

C4. Third National Congress of Physical Sciences, 29.09-2.10.2016, Sofia P5. 1-st ECMP, September 1-4, 2016, Athens, Greece